

# Ultrasensitive Electrochemical Sensor for the Detection of Mefenamic Acid Based on Calcium Vanadate Nanofilaments/Reduced Graphene Oxide Nanocomposite

Saranvignesh Alagarsamy<sup>1</sup>, Vinitha Mariyappan<sup>1</sup>, Shen-Ming Chen<sup>1,\*</sup>, Ruspika sundaresan<sup>1</sup>, Tse-Wei Chen<sup>1,2</sup>, Tien-Wen Tseng<sup>1,\*</sup>, Syang-Peng Rwei<sup>2,3</sup>, Jaysan Yu<sup>4</sup>

<sup>1</sup> Department of Chemical Engineering and Biotechnology, National Taipei University of Technology, No. 1, Section 3, Chung-Hsiao East Road, Taipei 106, Taiwan, ROC.

<sup>2</sup> Research and Development Center for Smart Textile Technology, National Taipei University of Technology, No.1, Section 3, Chung-Hsiao East Road, Taipei 106, Taiwan, ROC.

<sup>3</sup> Institute of Organic and Polymeric Materials, National Taipei University of Technology, Taiwan.

<sup>4</sup> Well Fore special wire corporation, 10, Tzu-Chiang 7rd., Chung-Li Industrial Park, Taoyuan, Taiwan

\*E-mail: [smchen78@ms15.hinet.net](mailto:smchen78@ms15.hinet.net) (S.M.Chen), [f10403@ntut.edu.tw](mailto:f10403@ntut.edu.tw) (T.W.Tseng)

Received: 2 March 2022 / Accepted: 6 April 2022 / Published: 7 May 2022

In this work, we successfully developed the Ca<sub>10</sub>V<sub>6</sub>O<sub>25</sub> (CVO) nanofilaments embedded reduced graphene oxide (RGO) nanocomposite by the facile hydrothermal method and fabricated on the surface of the working electrode (glassy carbon electrode-GCE), which is used for the detection of mefenamic acid (MFA). It is highly selective, more sensitive, and low-cost. Our hydrothermally prepared CVO/RGO nanocomposite was scrutinized by various spectroscopies. The electrical conductivity of the CVO nanofilaments was enhanced by the RGO nanosheets, which were established by EIS and CV analysis. our proposed CVO/RGO/GCE sensor displayed excellent sensitivity and selectivity for the detection of MFA. Furthermore, our proposed CVO/RGO/GCE sensor exhibited a low detection limit (LOD) of 0.0079 μM. Additionally, we scrutinized the practical application of our proposed CVO/RGO/GCE sensor towards MFA in the real samples (human blood serum and urine) which displayed good recovery results.

**Keywords:** Nonsteroidal anti-inflammatory drugs; Hydrothermal; Bimetal oxides; Cyclic voltammetry; Mefenamic acid;

## 1. INTRODUCTION

In recent years, the pharmaceutical industry has grown rapidly due to the rapid increase of the world population, which has inevitably caused new biomedical and environmental issues[1, 2]. Pharmaceutical chemicals can enter the aquatic environment through human and animal excretion as active metabolites as well as unmetabolized forms[3]. Medicines called nonsteroidal anti-inflammatory

drugs (NSAIDs) are usually consumed to decrease pain and inflammation and to bring down a high temperature[4]. Mefenamic acid (MFA) is an important NSAID, which is taken for the immediate treatment of mild to moderate pain from various conditions, mainly consumed to reduce blood loss and pain during menstrual periods[5]. MFA is generally safe to use at a normal dose for public health, but long-term or large doses can lead to harmful impacts on human health such as diarrhea, headache, nervousness, constipation, vomiting, stomach pain, fever, anemia, etc[6, 7]. Moreover, according to current monitoring studies, NSAID concentrations in the freshwater ecosystem range from ng/L to  $\mu\text{g/L}$ , creating numerous threats to non-target aquatic animals[8]. Therefore other than pharmaceutical quality control, there is a serious requirement for selective, sensitive, and portable methods to monitor the MFA residues in biological and environmental water samples. Previously various methods had been developed for the detection of MFA, such as chemiluminescence[9], high-performance liquid chromatography (HPLC)[10], spectrophotometry[11], capillary electrophoresis[12], flow injection analysis[13], spectrofluorimetric[14] ,etc. However, the above-mentioned methods are expensive and time-consuming, therefore we require a simple, cost-effective, and quick-response approach. As a result, here we have selected the electrochemical sensor for MFA detection since it is a less expensive, and portable approach that provides a rapid response to the target. Numerous studies have previously reported on the electrochemical sensor detection of MFA[15-18]. Based on the earlier reported sensors, we still need a more sensitive, and efficient sensor to detect MFA.

To improve the detection level and accuracy, choosing a good electrode material is extremely important. Currently, bimetal oxides (BMOs) are extremely used in several research fields, such as water splitting[19], battery materials[20], solar cells[21], photocatalysts[22], supercapacitors[23], electrochemical sensors[24], etc. Moreover, BMOs have high attention in the field of removal of environmental contamination [25]. Generally, BMOs have excellent conductivity, high durability, and large numbers of reactive sites. Nowadays, ternary metal vanadates have been used in several scientific research due to their strong optical, and electrochemical properties[24][26]. Significantly calcium vanadium oxides (CVO) exhibits potential application in lithium batteries[27], optical devices[28], magnetism[29], and electrochemical sensors[30]. Especially,  $\text{Ca}_{10}\text{V}_6\text{O}_{25}$  (CVO) has received more attention, due to its geometric structure, in which both Ca and V cations adopt different local coordinations. The CVO was previously prepared by different techniques such as coprecipitation and microwave-assisted hydrothermal methods[32]. Generally, carbon-based materials enhanced the electrocatalytic property of BMOs, according to previous reports, carbon-based materials(graphene, graphene oxide, carbon nanofiber, carbon nanotube, graphene aerogel) have great electrical conductivity, unique physical and chemical properties, high mechanical strength, high surface area, quick electron transfer, and is low-cost[33-35]. Especially, RGO has inherent catalytic properties, with excellent chemical stability[36]. Additionally, more functional groups exist on its surface, it is beneficial for the interaction of the CVO nanofilaments and RGO nanosheets.

Herein we report, that the CVO/RGO nanocomposite was successfully prepared by the facile hydrothermal method and fabricated on the surface of a glassy carbon electrode (GCE) for the detection of MFA. The hydrothermally prepared CVO/RGO nanocomposite was scrutinized by various spectroscopy studies such as field emission scanning electron microscopy (FESEM), powder X-ray diffraction analysis (XRD), and micro-Raman spectroscopy. The electrical conductivity of the

CVO/RGO nanocomposite was examined by electrochemical impedance spectroscopy (EIS) and the electrochemical performance towards the MFA was explored by cyclic voltammetry (CV) and differential pulse voltammetry (DPV). The obtained DPV results exhibited excellent selectivity and sensitivity, good stability, a wide linear range, and low LOD. Hence the obtained results establish that CVO/RGO/GCE sensor was well suitable for the detection of MFA. Moreover, we used CVO/RGO/GCE sensor for the detection of MFA in biological samples, which exhibited good recovery results. Hence, our proposed sensor is more favorable for the detection of MFA in biological samples such as human blood serum and urine.

## 2. EXPERIMENTAL SECTION

### 2.1. Materials and reagents

Graphite powder (<20  $\mu\text{m}$ ), ammonium metavanadate ( $\text{NH}_4\text{VO}_3$ ,  $\geq 99.9\%$ ), calcium chloride dihydrate ( $\text{CaCl}_2 \cdot 2\text{H}_2\text{O}$ ,  $\geq 99.9\%$ ), potassium hydroxide (KOH,  $\geq 85\%$ , pellets), sodium hydroxide (NaOH,  $\geq 98\%$ , pellets (anhydrous)), sodium phosphate dibasic ( $\text{Na}_2\text{HPO}_4$ ), sodium phosphate monobasic ( $\text{NaH}_2\text{PO}_4$ ), mefenamic acid ( $\text{C}_{15}\text{H}_{15}\text{NO}_2$ ) were purchased as the analytical grade from Sigma-Aldrich and utilized directly without any purification. The 0.1 M phosphate buffer (PB) was used as the supporting electrolyte. We collected human blood serum and urine from Chang Gung Memorial Hospital, Taiwan, for the real sample analysis.

### 2.2. Instrumentation

The crystallographic structure of all prepared samples was studied by the powder x-ray diffraction (XRD, XPERT-PRO, PAN analytical B.V., The Netherlands) and the diffractometer with  $\text{Cu K}\alpha$  radiation ( $k = 1.54 \text{ \AA}$ ). The structural morphology of the prepared nanocomposite was taken by field emission scanning electron microscopy (FESEM, Hitachi S-3000 H), scanning electron microscopy (SEM, JSM-6510). Raman data was collected from the Micro-Raman spectrometer. The electrical conductivity of the prepared samples was investigated by the electrochemical impedance spectroscopy (EIS), and electrochemical performance was recorded in the electrochemical work station such as cyclic voltammetry (CV CHI 1205a), and differential pulse voltammetry (DPV, CHI900), CH Instruments company, made in the U.S.A. Overall experiments were performed in the three-electrode system a saturated Ag/AgCl was used as a reference electrode, the platinum wire was used as a counter electrode and a glassy carbon electrode (GCE) was used as a working electrode (electrode surface area =  $0.071 \text{ cm}^2$ ).

### 2.3. Synthesis of graphene oxide (GO):

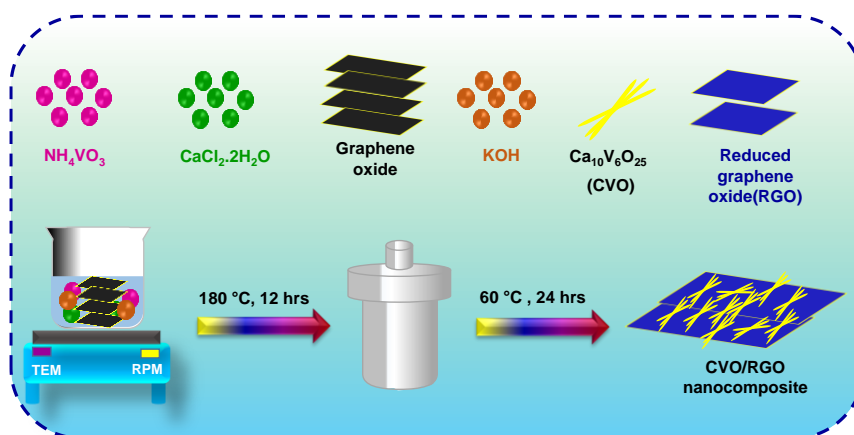
GO was initially prepared from graphite powder using the modified Hummers approach, according to a previously published method[33]. Then, the prepared GO was utilized for the synthesis of the CVO /RGO nanocomposite.

#### 2.4. Synthesis of CVO/RGO nanocomposite

The CVO/RGO nanocomposite was prepared by the facile hydrothermal method. At first 0.5 g of  $\text{NH}_4\text{VO}_3$ , 0.5 g of  $\text{CaCl}_2 \cdot 2\text{H}_2\text{O}$  and 0.5 g of previously prepared GO were taken and dissolved in 70 ml of DI water, which is stirred under a magnetic stirrer at 50 °C for 1 hour. Then pH of the reaction mixture was adjusted to 12 via dropwise addition of 0.1 M KOH solution under room temperature. Finally, the reaction mixture was fully transferred into the 100 ml Teflon-lined stainless-steel autoclave, which was heated in a muffle furnace at 180 °C for 12 hrs. At the end of the reaction, the autoclave was allowed to cool at room temperature. After centrifugation, the collected product was washed with DI water and ethanol, then dried at 60 °C for 24 hrs. Later, the obtained CVO/RGO nanocomposite was directly used for further electrochemical investigations. A similar method was followed for the preparation of CVO without the addition of GO. The RGO was prepared by reducing GO with ascorbic acid (AA), which was prepared by our previously reported article[33]. The prepared RGO and CVO were used for further electrochemical comparison studies.

#### 2.5. Modification of glassy carbon electrode (GCE)

Initially, the bare GCE surface was polished with alumina on metallographic sandpaper, after the GCE surface was completely cleaned with DI water and ethanol then the prepared bare GCE was dried at 50 °C for 15 mins. Subsequently, 10 mg of CVO/RGO nanocomposite was dispersed in 10 ml DI water to get a homogeneous dispersion solution, which was sonicated for 30 min. Then the dispersion solution was coated on a clean polished mirror-like surface of bare GCE then it dried at 50 °C for 30 mins and which is used for further electrochemical investigations. The same approach was used to modify the other electrodes such as CVO/GCE and RGO/GCE for comparison studies. **Scheme.1.** displayed the graphical representation for the synthesis of CVO/RGO nanocomposite.



**Scheme.1.** Illustrate the hydrothermal synthesis procedure of CVO/RGO nanocomposite.

### 3. RESULT AND DISCUSSION

#### 3.1 Morphological Characterization of CVO/RGO nanocomposite

Fig.1.(a) displays the magnifying FE-SEM image of CVO nanoparticles, the obtained image established that our prepared CVO nanoparticles are self-assembled and formed the nanofilaments as a bundle of straw shape, which is randomly oriented in all directions. Fig.1.(b) displays the FE-SEM image of RGO, it confirms the wrinkled edges of RGO are extremely folded paper-like format. Fig.1.(c and d) displays the magnifying FE-SEM images of CVO/RGO nanocomposite, CVO nanofilaments are finely connected to the RGO surface, and the CVO nanofilaments are covered by the RGO nanosheets. Moreover, the RGO nanosheet improves the conductivity and electrochemical property of CVO nanofilaments. Fig.1.(e-i) shows the FESEM elemental mapping of the CVO/RGO nanocomposite, it proves the existence of Ca, V, O, and C in the CVO/RGO nanocomposite. Fig.1.(j) shows the EDX spectra of CVO/RGO nanocomposite that was purer with the compositions of 26.3 % Ca, 19.9 % V, 23.2 % O, and 30.6 % C. The above-mentioned results confirm the effective formation of the CVO/RGO nanocomposite.

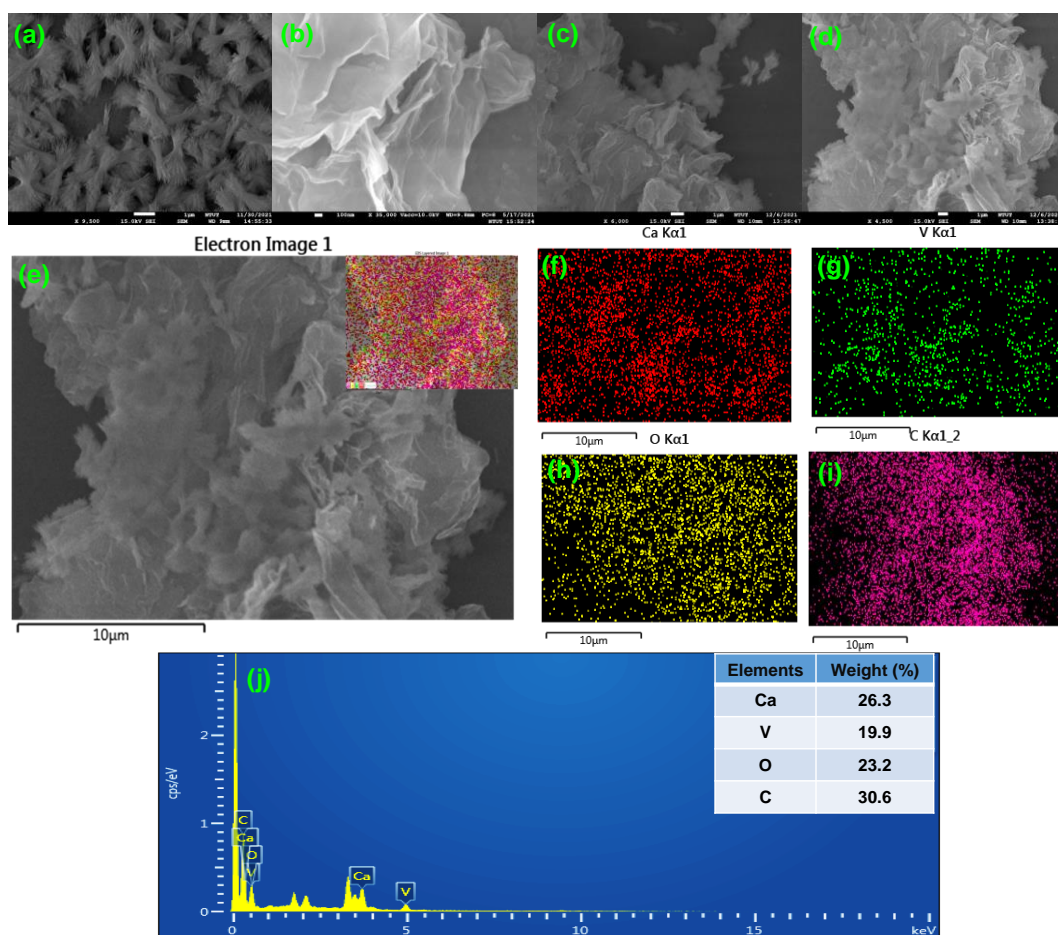


**Figure 1.** (a) The FESEM images of CVO nanofilaments (b) RGO nanosheet, and (c and d) CVO/ RGO nanocomposite, (e-i) FESEM-EDS mapping of FESEM [(e) FESEM image of FESEM (insert: mixer of Ca, V, O, and C), (f) Ca (g) V (h) O (i) C], (j) EDX spectrum, insert; the elemental percentage of Ca, V, O, and C in the nanocomposite.

### 3.2. Structural characterization of CVO/RGO nanocomposite

Fig.2. (a) shows the XRD diffraction peak patterns of CVO and CVO/RGO. The hydrothermally prepared CVO exhibited the diffraction peaks positioned at  $2\theta$  angles of  $53.38^\circ$ ,  $22.19^\circ$ ,  $25.41^\circ$ ,  $30.74^\circ$ ,  $31.42^\circ$ ,  $33.20^\circ$ ,  $38.38^\circ$ ,  $45.27^\circ$ ,  $48.24^\circ$ ,  $52.19^\circ$ ,  $62.39^\circ$ , and  $74.91^\circ$ , these are corresponding to the plane of (104), (111), (002), (211), (112), (202), (310), (222), (213), (004), (304), and (611) respectively. The obtained diffraction peaks were well matched with the (JCPDS. card no. 00-052-0649) hexagonal crystal system of  $\text{Ca}_{10}\text{V}_6\text{O}_{25}$  [37]. The CVO/RGO nanocomposite also exhibited similar diffraction peaks of CVO and it exhibited a diffraction peak at  $25.41^\circ$ , which is corresponding to the (002) plane. The presence of the (002) plane confirms the existence of RGO in the CVO/RGO nanocomposite. Therefore the obtained XRD results confirm the effective formation of CVO/RGO nanocomposite.

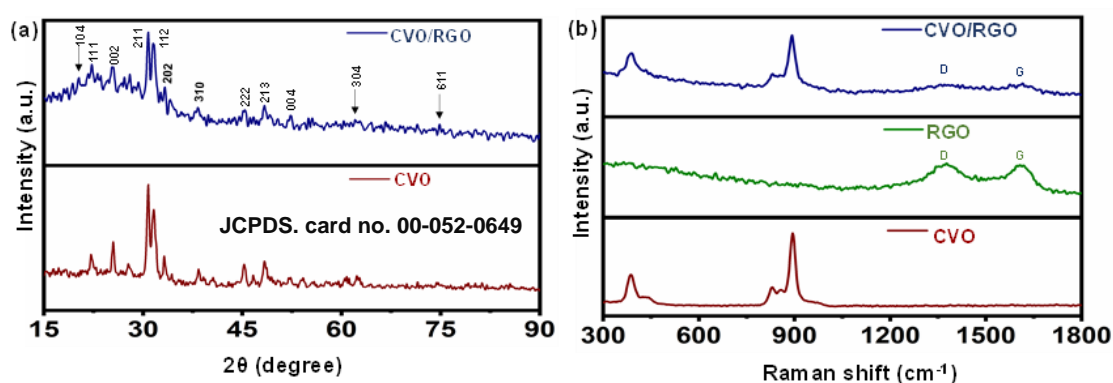


**Figure 2.** (a) The comparison of XRD patterns of CVO, and CVO/RGO nanocomposite, and (b) the Raman spectra for CVO, RGO, and CVO/RGO nanocomposite.

The Raman spectra of CVO, RGO, and CVO/RGO nanocomposite were displayed in **Fig.2(b)**. The CVO exhibited the Raman peaks at  $128\text{ cm}^{-1}$ ,  $244\text{ cm}^{-1}$ ,  $387\text{ cm}^{-1}$ ,  $433\text{ cm}^{-1}$ ,  $828\text{ cm}^{-1}$ ,  $894\text{ cm}^{-1}$ , and  $969\text{ cm}^{-1}$ , these peaks were associated with the lattice modes of  $[\text{CaO}_6]$  clusters, bending vibration of the O–V–O bond, stretching vibration of the V–O bond and symmetric stretching vibrations of the  $[\text{VO}_4]$  cluster[28]. The obtained result was closely matched with the previously reported data. The RGO exhibited the two dominant Raman peaks at nearly  $1350\text{ cm}^{-1}$  and  $1580\text{ cm}^{-1}$ , which are corresponding to the D and G bands. The D band is caused by out-of-plane vibrations connected with structural defects, and the G band is caused by in-plane vibrations of  $\text{sp}^2$  connected carbon atoms[38]. The intensity ratio of the D band to the G band ( $I_D/I_G$ ) was used to calculate the disorder degree of carbon-based materials. The calculated ( $I_D/I_G$ ) values for the RGO and CVO/RGO were 0.99, and 1.0 respectively, which exposed the  $I_D/I_G$  ratio of CVO/RGO is comparatively higher than the RGO due to the incorporation of CVO nanofilaments on the surface of the RGO nanosheet. At the same time, CVO/RGO exhibited the Raman peaks of CVO also. Hence these results indicated that higher defects, existed in the CVO/RGO nanocomposite.

## 3.3. Electrochemical impedance spectroscopic (EIS) study

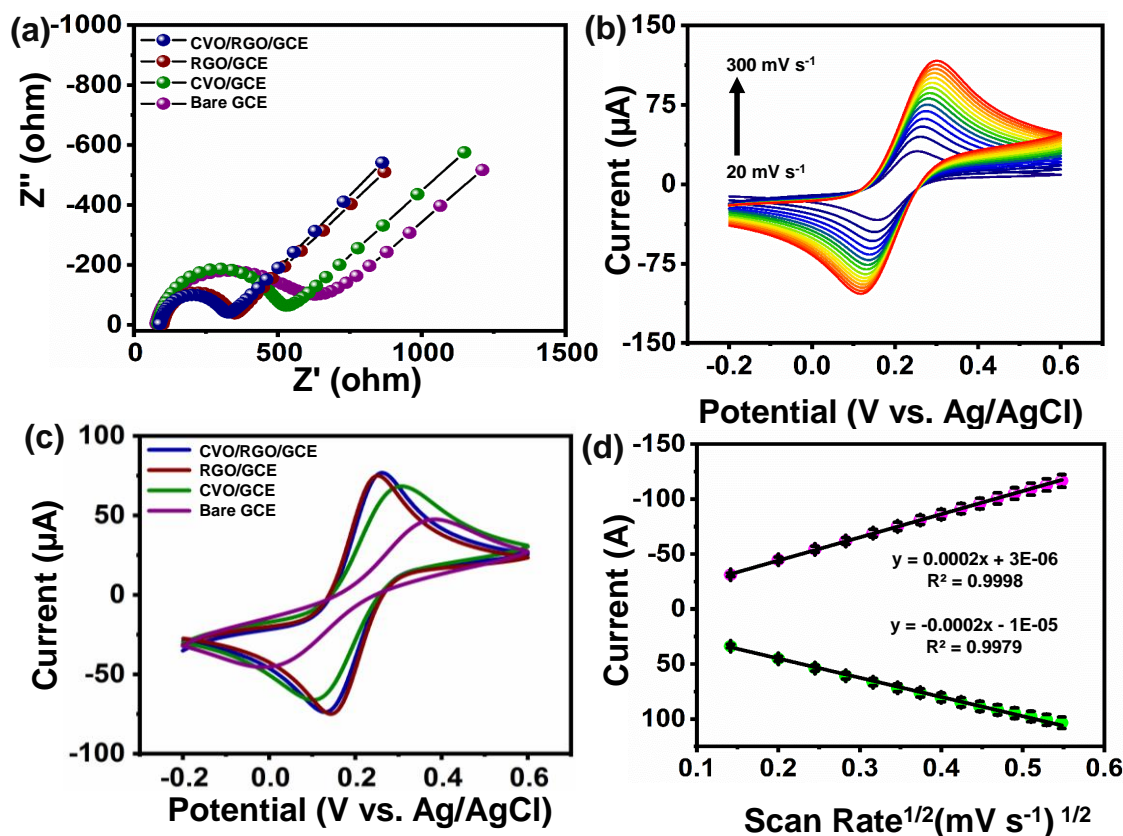


**Figure 3.** (a) EIS plots for the bare GCE, CVO/GCE, RGO/GCE, and CVO/RGO/GCE (b) CV redox current curves for the bare GCE, CVO/GCE, RGO/GCE, and CVO/RGO/GCE, at a scan rate  $50 \text{ mV s}^{-1}$ , (c) CV redox current curves for the CVO/RGO/GCE at scan rate from  $20$  to  $300 \text{ mV s}^{-1}$ , and (d) the corresponding linear plot for redox current response versus the square root of scan rates. All of these experiments were performed in a  $5 \text{ mM } [\text{Fe}(\text{CN})_6]^{3-/4-}$  with  $0.1 \text{ M KCl}$  solution.

The electron transfer properties of the modified electrode surface were investigated by electrochemical impedance spectroscopy (EIS) analysis. The EIS analysis was utilized to examine the electrode surface of the bare GCE and various modified electrodes such as CVO/GCE, RGO/GCE, and CVO/RGO/GCE. The EIS plot for the bare GCE, CVO/GCE, RGO/GCE, and CVO/RGO/GCE is displayed in **Fig.3.(a)**, which was performed in  $0.1 \text{ M KCl}$  solution containing  $5 \text{ mM}$  of  $[\text{Fe}(\text{CN})_6]^{3-/4-}$ . According to the EIS plot the  $R_{ct}$  (electron transfer resistance) values for the bare GCE, CVO/GCE, RGO/GCE, and CVO/RGO/GCE were calculated to be  $567$ ,  $444$ ,  $249$ , and  $240 \Omega$  respectively. As a result, the integration of CVO nanofilaments is reduced the  $R_{ct}$  value of RGO, therefore CVO/RGO modified GCE exhibited a small semi-circle with a low  $R_{ct}$  value. According to these results, CVO/RGO has good electrical contact between the electrode and electrolyte, and the presence of the RGO made the charge transfer easier because it has a large surface area.

The cyclic voltammetry (CV) was used to examine the catalytic activity of the prepared electrocatalyst[31]. The bare GCE and other modified GCEs were examined by the CV analysis, which is displayed in **Fig.5(b)**, This investigation was performed in  $0.1 \text{ M KCl}$  solution containing  $5 \text{ mM}$  of  $[\text{Fe}$

$(\text{CN})_6]^{3-/4-}$ . The obtained results exposed that the CVO/RGO/GCE has the highest redox peak current response, compared to the bare and other modified GCEs. Because CVO/RGO nanocomposite has a large surface area and more active sites. Therefore CVO/RGO/GCE has high electron transferability.

The CVO/RGO/GCE was evaluated by CV with different scan rates, as shown in **Fig.3.(c)**, and the analysis was carried out in 0.1 M KCl solution containing 5 mM of  $[\text{Fe}(\text{CN})_6]^{3-/4-}$  with scan rate increasing from 20 to 300  $\text{mVs}^{-1}$ . The dependence linear plot for the redox peak currents and the square root of scan rates is displayed in **Fig.3.(d)**. The obtained results exposed that the CVO/RGO/GCE has strong redox peak current responses, as well as excellent linear plots for redox current response against the square root of scan rates. The Randles-Sevcik Equation (1)[45], was used to determine the electrochemical active surface area (EASA) of the redox process,

$$I_p = (2.69 \times 10^5) n^{3/2} D^{1/2} A v^{1/2} C \quad (1)$$

Where  $I_p$  is the peak current value,  $v$  is the scan rate,  $D$  is the diffusion coefficient,  $C$  is the bulk concentration of  $[\text{Fe}(\text{CN})_6]^{3-/4-}$ , and  $n$  is the number of electrons involved in the electrochemical reaction. The aforementioned equation (1), was used to calculate the EASA values of the bare GCE, CVO/GCE, RGO/GCE, and CVO/RGO/GCE the resulting EASA values were calculated to be 0.038, 0.054, 0.072, and 0.078  $\text{cm}^2$  respectively. The obtained results revealed that CVO/RGO/GCE had a higher EASA value because the CVO/RGO nanocomposite has more active sites and a large surface area[44]. The combination of CVO nanofilaments and the RGO enhanced the quick electron transfer because which is mainly depends on the synergistic effect between the CVO nanofilaments and the RGO nanosheets, which was confirmed by the EIS analysis. According to the results, the greater EASA value of CVO/RGO/GCE is expected to be more beneficial for the detection of MFA.

### 3.4. Electrochemical detection of MFA

The electrochemical performance of CVO/RGO/GCE towards MFA was inspected by the cyclic voltammetry (CV) and differential pulse voltammetry (DPV) analysis. Primarily, the CV analysis was performed to inspect the coating effect of the CVO/RGO nanocomposite, on the surface of the GCE was modified with different concentrations of CVO/RGO (2, 4, 6, and 8  $\mu\text{L}$ ), and the CV analysis was recorded in the presence of 100  $\mu\text{M}$  MFA with 0.1 M PB (pH=7) at a scan rate of 50  $\text{mVs}^{-1}$  displayed in **Fig.4(a)**. According to the CV current response, the GCE modified with 6  $\mu\text{L}$  of CVO/RGO has a higher current response when compared to other modified electrodes. Therefore, the bare GCE was modified with a 6  $\mu\text{L}$  concentration of CVO/RGO nanocomposite and utilized for further electrochemical studies. **Fig.4(b)** displayed the corresponding bar graph for CV current response against different catalyst dosages ( $\mu\text{L}$ ).

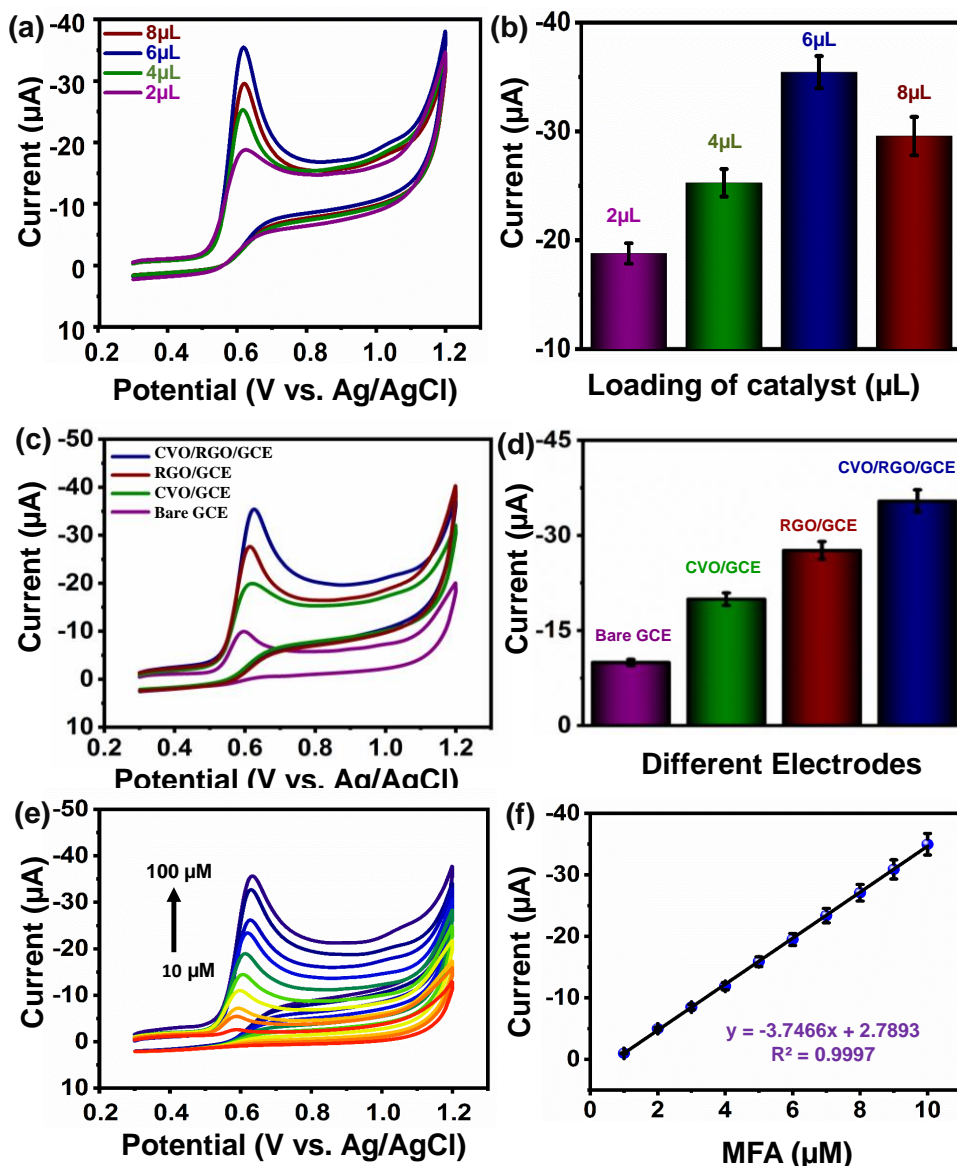


**Figure 4.** (a) The CV current curves for 100 μM of MFA at CVO/RGO/GCE with various amounts of catalyst (CVO/RGO) coating on GCE (2, 4, 6, and 8 μL) in the presence of N<sub>2</sub> gas, saturated 0.1 M PB (pH=7) at a scan rate of 50 mV s<sup>-1</sup>, and (b) the corresponding bar diagram for peak current versus the amount of catalyst CVO/RGO loading on GCE (μL), (c) CV current curve for the bare GCE, CVO/GCE, RGO/GCE, and CVO/RGO/GCE, in the presence of N<sub>2</sub> gas, saturated 0.1 M PB (pH=7) containing 100 μM MFA at a scan rate of 50 mV s<sup>-1</sup>, (d) the dependence bar graph for peak current versus different modified electrodes, (e) CV current curve of CVO/RGO/GCE at various concentrations of MFA (10-100 μM) with N<sub>2</sub> gas saturated 0.1 M PB (pH=7) at a scan rate 50 mV s<sup>-1</sup>, and (f) the corresponding linear plot for the peak currents against different concentrations of MFA.

**Fig.4(c)** CV current curves show the comparison electrochemical response towards MFA, for the bare GCE, CVO/GCE, RGO/GCE, and CVO/RGO/GCE, in the presence of N<sub>2</sub> gas, saturated 0.1 M PB (pH=7) with 100 μM MFA at a scan rate of 50 mV s<sup>-1</sup>. The obtained results revealed that the MFA reaction is the irreversible oxidation process. **Fig.4(d)** shows the dependence bar graph for peak current

value versus different modified GCEs. According to the obtained results, the CVO/RGO modified GCE exhibits a higher peak current when compared to the bare and other modified GCE because it has more active sites, a large surface area, and great electron transferability. The CVO nanofilaments were attached to RGO through the strong electrostatic interaction, and the synergistic effect between the CVO and RGO, which exposed the novel synergistic properties and surely helps the rapid electron transfer. The catalytic property of CVO nanofilaments was improved by the RGO nanosheets and the CVO/RGO nanostructure was also advantageous for the electrochemical detection of MFA.

The CV current response of CVO/RGO/GCE at various concentrations of MFA (10 to 100  $\mu\text{M}$ ) with  $\text{N}_2$  gas saturated 0.1 M PB (pH=7) at a scan rate of  $50 \text{ mV s}^{-1}$  is shown in **Fig.4(e)**. The obtained results revealed that as the concentration of MFA was increased from 10 to 100  $\mu\text{M}$ , the peak current response also increased gradually, which established the rapid electron transfer of the CVO/RGO nanocomposite. **Fig.4(f)** shows the dependence linear plot for the peak currents versus different concentrations of MFA and exposed a good linear regression equation with the coefficient value for the peak currents  $I_p(\mu\text{A}) = -3.7466 (\text{MFA}) (\mu\text{M}) + 2.7893$ ,  $R^2 = 0.9997$  respectively.

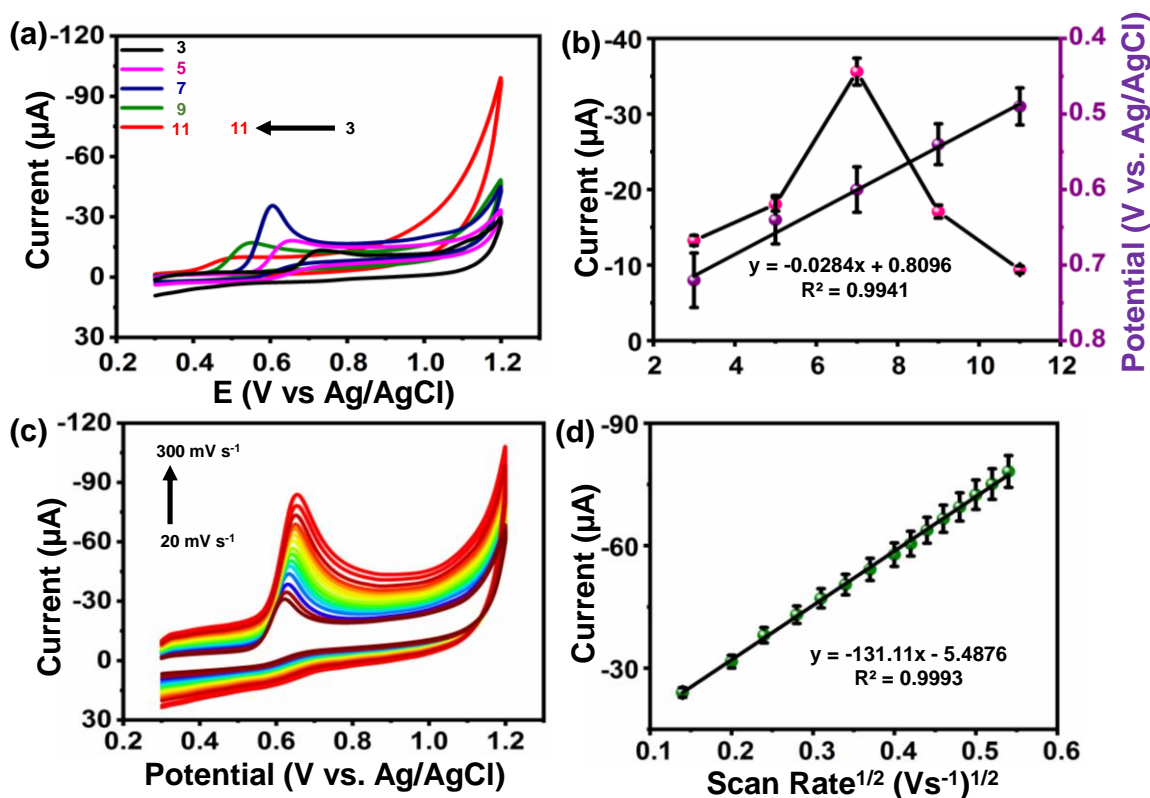


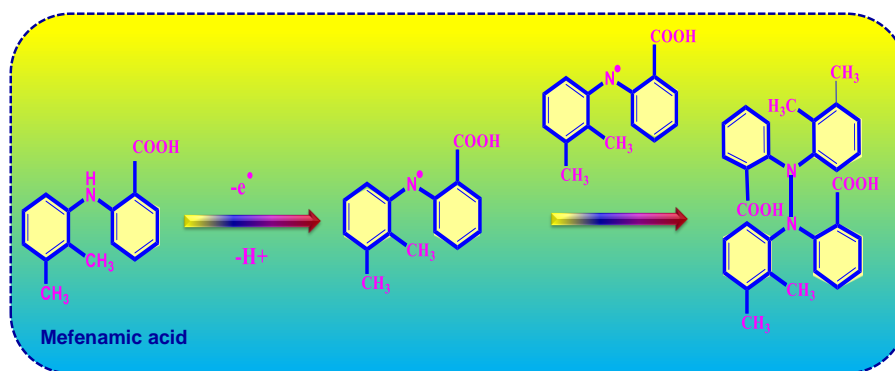
**Figure 5.** (a) CV current response of 100  $\mu\text{M}$  of MFA at CVO/RGO/GCE with different pH (3.0, 5.0, 7.0, 9.0, and 11.0) under  $\text{N}_2$  gas saturated PB at scan rate  $50 \text{ mV s}^{-1}$ , and (b) the corresponding linear plot for different pH versus potential and current, (c) CV current response of CVO/RGO/GCE at various scan rates (20–300  $\text{mV s}^{-1}$ ) in  $\text{N}_2$  gas saturated 0.1 M PB (pH=7) with 100  $\mu\text{M}$  of MFA, and (e) the dependence linear plot for peak currents versus the square root of scan rates.

The effect of pH was scrutinized at CVO/RGO/GCE in the presence of N<sub>2</sub> gas saturated various pH ranges (3.0-11.0) electrolyte containing 100 μM of MFA by CV study, as shown in **Fig.5(a)**. According to the result, pH=7 has the highest peak current response compared to the other electrolytes, therefore pH=7 was preferred as the supporting electrolyte for further electrochemical studies. **Fig.5(b)** displays the dependence plot for pH against current and potential, then the pH value and peak potential exhibited a great linear plot with regression equation and coefficient value  $E_p$  (V) = -0.0284 (pH) + 0.8096 and  $R^2 = 0.9941$  respectively. The resultant equation's slope value was applied in the Nernst equation (2),

$$E_p = - \left( \frac{0.0591m}{n} \right) \text{pH} + b \quad (2)$$

Where m and n are the number of protons and electrons involved in the electrochemical reaction, equation (2) was used to calculate the m/n ratio of MFA is 0.48, which suggested that an equivalent number of protons and electrons are contributing to the irreversible electrochemical oxidation process of MFA at CVO/RGO/GCE. The previous studies exposed that the irreversible oxidation process of MFA involves the transfer of two electrons and two protons. **Scheme.2.** displays the plausible electro-oxidation mechanism of MFA[39].

The kinetic property of CVO/RGO/GCE was scrutinized by the different scan rate studies, **Fig.5(c)** shows the CV current curves of CVO/RGO/GCE carried out in the presence of N<sub>2</sub> gas saturated 0.1 M PB (pH=7) with 100 μM MFA at different scan rates (20 to 300 mV s<sup>-1</sup>). **Fig.5(d)** shows the corresponding linear plot for peak current against the square root of scan rates with coefficient value and linear regression equation  $R^2 = 0.9993$ , and  $I_p$  (μA) = -131.11(Vs<sup>-1</sup>)<sup>1/2</sup> -5.4876 respectively. According to the result, CV current values were increased when increasing the scan rates, and the CV peaks slightly shifted to the positive side. The obtained result revealed the electrochemical oxidation reaction of MFA at the CVO/RGO/GCE process was a diffusion-controlled process.



**Scheme 2.** The plausible electro-oxidation mechanism of MFA.

### 3.5. DPV determination of MFA

DPV is a quantitative technique, it has greater sensitivity than CV [46]. Hence our proposed CVO/RGO/GCE electrochemical sensor was examined by the DPV analysis, to detect the MFA. **Fig. 6(a)** displays the DPV response of CVO/RGO/GCE for the constant addition of various concentrations

of MFA (0.001–425  $\mu\text{M}$ ) under  $\text{N}_2$  gas saturated 0.1 M PB (pH=7). The peak current response increases rapidly after each addition of MFA.

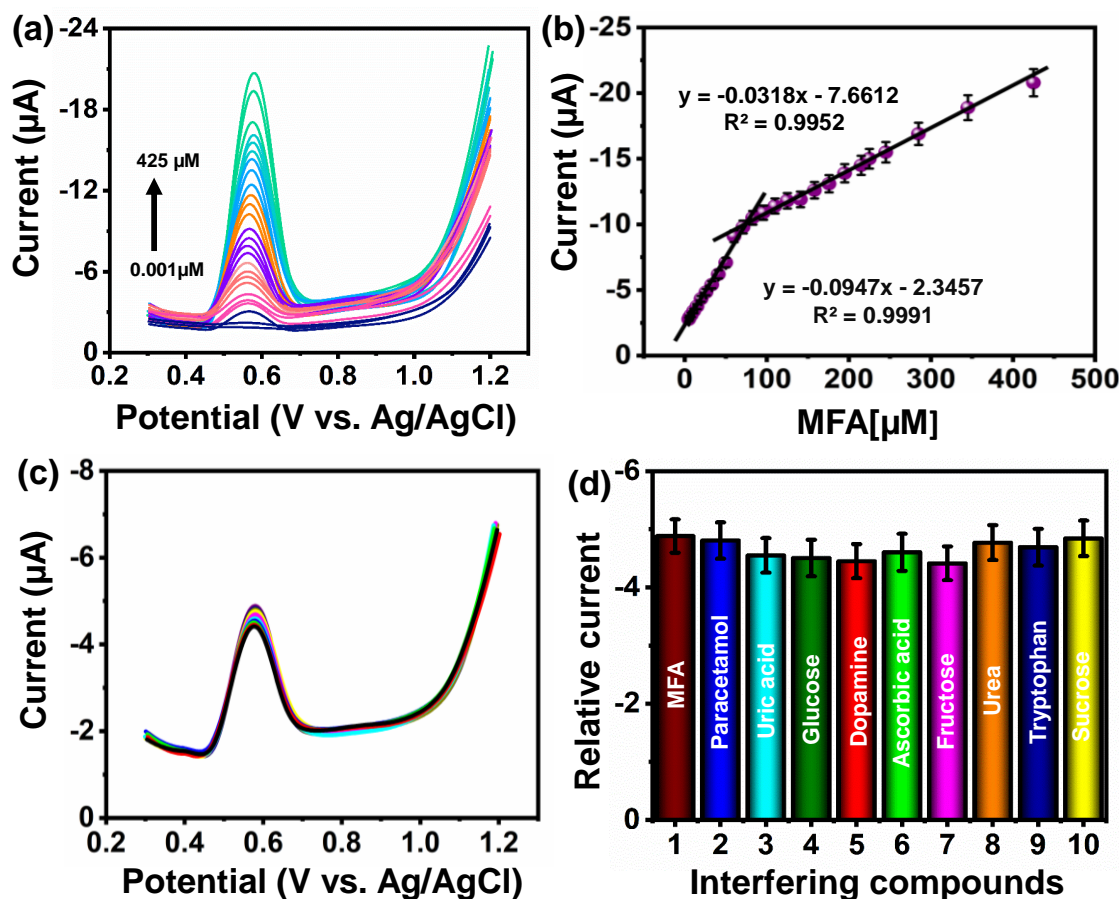


**Figure 6.** (a) DPV current curves of the CVO/RGO/GCE with various concentrations of MFA (0.001–425  $\mu\text{M}$ ) in  $\text{N}_2$  gas saturated 0.1 M PB (pH=7), (b) the corresponding linear plot for DPV current response against concentrations of MFA, (c) the DPV current response of CVO/RGO/GCE for 100  $\mu\text{M}$  MFA with some potential interfering species (2-10), in  $\text{N}_2$  gas saturated 0.1 M PB (pH=7), and (d) The dependence bar diagram of relative current against interfering compounds.

The obtained DPV current curves of CVO/RGO/GCE were linearly plotted with the wide concentration of MFA displayed in **fig. 6(b)**, according to the result which exposed two excellent linear regression equations and the coefficient values for the lower and higher concentrations of MFA,  $I_p$  ( $\mu\text{A}$ ) =  $-0.0947[\text{MFA}]$  ( $\mu\text{M}$ ) - 2.3457,  $R^2 = 0.9991$ , and  $I_p$  ( $\mu\text{A}$ ) =  $-0.0318[\text{MFA}]$  ( $\mu\text{M}$ ) - 7.6612,  $R^2 = 0.9952$  respectively. The limit of detection (LOD) was determined to be 0.0079  $\mu\text{M}$  by the standard equation,  $\text{LOD} = 3 S/q$ , where 'q' is the slope value ( $0.0947 \mu\text{A} \mu\text{M}^{-1}$ ) from the calibration plot, and 'S' is the standard deviation obtained from the five measurements of the blank signal ( $0.000252 \mu\text{A}$ ). Additionally, our proposed CVO/RGO/GCE sensor exhibited a good sensitivity of  $1.333 \mu\text{A} \mu\text{M}^{-1} \text{cm}^{-2}$ . Furthermore, the CVO/RGO/GCE sensor for the detection of MFA was compared with those earlier reported MFA sensors in the terms of linear range and LOD as displayed in **Table 1**. When compared to the previously

reported sensors our proposed CVO/RGO/GCE sensor exposed low LOD and a wide linear range for the detection of MFA.

**Table 1.** The electrochemical detection of MFA at CVO/RGO/GCE is compared to the previously reported electrodes.

Electrodes	LOD ( $\mu\text{M}$ )	Linear range ( $\mu\text{M}$ )	Methods	Reference
<sup>a</sup> CV/ <sup>b</sup> CPE	0.00234	0.01–470	<sup>l</sup> DPV	[39]
<sup>c</sup> MWCNTs/ <sup>d</sup> RuTiO <sub>2</sub> -CPE	0.00045	0.01 –0.9	<sup>m</sup> SWV	[18]
<sup>e</sup> CdO/ <sup>f</sup> PANI/ <sup>g</sup> mpg-C <sub>3</sub> N <sub>4</sub> / <sup>h</sup> GCE	0.045	0.2–400	DPV	[40]
<sup>i</sup> SWNT/GCE	0.0134	0.1–35	SWV	[41]
<sup>j</sup> Cu <sup>2+</sup> Y/ZMCPE	0.04	0.3–100	DPV	[42]
<sup>k</sup> MMW/CPE	0.0012	0.002–1.0	DPV	[43]
CVO/RGO/GCE	0.0079	0.001-425	DPV	<b>This work</b>

<sup>a</sup>CV:Cu<sub>5</sub>V<sub>2</sub>O<sub>10</sub>; <sup>b</sup>CPE :carbon paste electrode; <sup>c</sup>MWCNTs: multiwalled carbon nanotubes; <sup>d</sup>RuTiO<sub>2</sub>:rutheniumdoped titanium dioxide; <sup>e</sup>CdO: cadmium oxide; <sup>f</sup>PANI:polyaniline; <sup>g</sup>mpg-C<sub>3</sub>N<sub>4</sub>:mesoporous polymeric graphitic-carbon nitride; <sup>h</sup>GCE:glassy carbon electrode; <sup>i</sup>SWNT: single walled carbon nanotubes; <sup>j</sup>Cu<sup>2+</sup>Y/ZMCPE: copper(II) doped zeolite modified carbon paste electrode; <sup>k</sup>MMW: magneto multiwalled carbon nanotube; <sup>l</sup>DPV:differential pulse voltammetry; <sup>m</sup>SWV:square wave voltammetry.

### 3.6. Selectivity study of CVO/RGO/GCE

The selectivity of our proposed CVO/RGO/GCE sensor was examined in the DPV technique against consecutive injections of 100  $\mu\text{M}$  (1) MFA and 100-fold excess concentration of interferences such as (2) paracetamol, (3) uric acid, (4) glucose, (5) dopamine, (6) ascorbic acid, (7) fructose, (8) urea, (9) tryptophan, and (10) sucrose, under in the presence of N<sub>2</sub> gas saturated in 0.1 M PB displayed in **Fig.6(c)**. According to the DPV results, the current response and peak potential didn't affect by the addition of a 100-fold excess concentration of interferences, it confirms our proposed sensor has more selectivity toward MFA in the presence of other interferents. Each measurement was recorded thrice and the relative standard deviation (RSD) was calculated. All RSD values of the measured currents were under 10 %, which exposed that the determination of MFA with the CVO/RGO/GCE sensor was unaffected by the presence of other interferents. **Fig.6(d)** displays the bar graph for the current response and the interfering molecules.

## 3.7. Reproducibility, repeatability, and stability studies

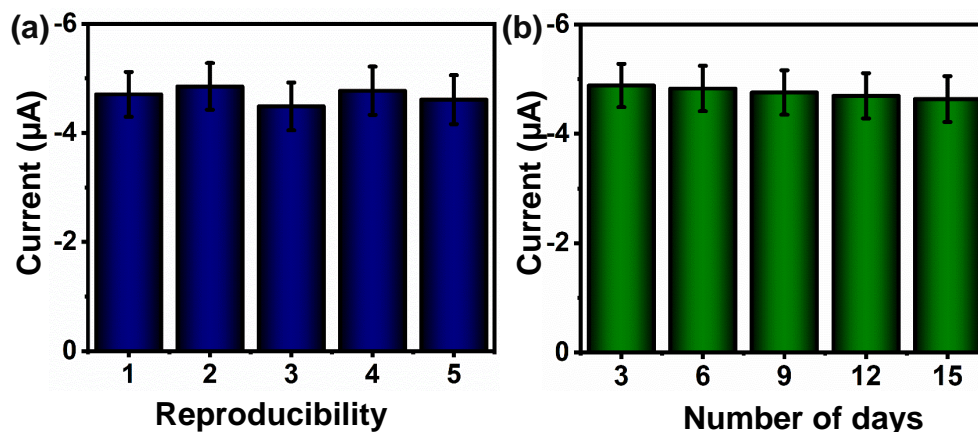


**Figure 7.** (a) The bar diagram for the current response of 5 independent CVO/RGO/GCE with 100  $\mu\text{M}$  of MFA in 0.1 M PB (pH=7), and (b) the bar diagram for the stability of the CVO/RGO/GCE with 100  $\mu\text{M}$  of MFA in 0.1 M PB (pH=7) over 15 days.

**Fig.7(a)** displays the bar diagram of five different CVO/RGO modified electrodes versus the DPV current response, which was performed in the presence of  $\text{N}_2$  gas saturated 0.1 M PB (pH=7), with 100  $\mu\text{M}$  of MFA, and the relative standard deviation (RSD) was determined to be 3.6 %, according to the result CVO/RGO/GCE has excellent reproducibility. The long-term electrochemical stability of the CVO/RGO/GCE sensor was investigated by DPV analysis, the CVO/RGO/GCE was performed in the presence of  $\text{N}_2$  gas saturated 0.1 M PB (pH=7), with 100  $\mu\text{M}$  of MFA, the current response of CVO/RGO/GCE monitored for 15 days, **Fig.7(b)** shows the bar diagram for the number of days and DPV current response of CVO/RGO/GCE. The investigations were recorded every day and the electrode was kept in a refrigerator at 5  $^\circ\text{C}$ . The retained current of about 96.3 % was obtained from its initial DPV experiment, which established the outstanding stability of the CVO/RGO/GCE sensor.

## 3.8. Real sample analysis

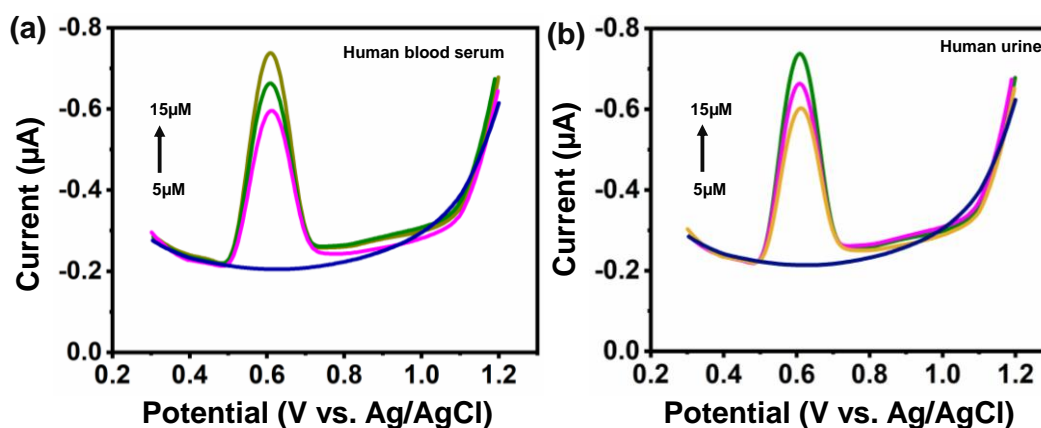


**Figure 8.** The detection of MFA in (a) human blood serum, and (b) urine samples.

We evaluated the practical applicability of our proposed sensor by using DPV analysis with a standard addition method in human blood serum and urine samples. Initially, the collected human blood serum and urine samples were diluted with N<sub>2</sub> gas saturated 0.1M PB (pH=7.0), which is directly used for the DPV analysis, The observed result revealed the absence of MFA in the real sample. Then the known concentration of MFA (5.0,10.0, and 15.0  $\mu$ M) was added to the real samples and the results were displayed in **fig. 8(a and b)** for human serum and urine sample respectively. The obtained recovery percentage and RSD values were displayed in **Table .2**. The obtained recovery results established that our proposed sensor can be used as an accurate and efficient sensing platform for the detection of MFA in real samples.

**Table 2.** The determination of MFA in human blood serum and urine sample at CVO/RGO/GCE.

Real samples	Added ( $\mu$ M)	Found ( $\mu$ M)	Recovery (%)	RSD*
Human blood serum	0	-	-	-
	5.0	4.93	98.6	3.0
	10.0	9.85	98.5	2.8
	15.0	14.92	99.4	3.1
urine sample	0	-	-	-
	5.0	4.96	99.2	2.8
	10.0	9.95	99.5	3.1
	15.0	14.8	98.6	3.0

\*Measurement of three experiments (n=3).

#### 4. CONCLUSION

Our proposed electrochemical sensor was based on CVO/RGO nanocomposite, which was successfully synthesized by the facile hydrothermal route and fabricated on the surface of GCE for the detection of MFA under optimized conditions. The large surface area and more active sites of CVO/RGO boost the adsorption of MFA. The CVO/RGO/GCE sensor exposed a quick response, low LOD, good sensitivity, robust reproducibility, long-term stability, and excellent selectivity. Furthermore, our proposed sensor was examined in the real samples for the detection of MFA which displayed satisfactory results. Hence overall findings of this current work suggested CVO/RGO is a promising material in the sensor platform.

#### CONFLICTS OF INTEREST

There are no conflicts to declare

## ACKNOWLEDGMENT

The authors are grateful for the financial support from the Ministry of Science and Technology (MOST), Taiwan, Project no. MOST 110–2113-M-027–007 and Project no. MOST 110–2113-M-027–003./4.0/).

## References

1. L. Qian, S. Durairaj, S. Prins, A. Chen, *Biosens. Bioelectron.*, 175 (2021) 112836.
2. N. Karuppusamy, V. Mariyappan, S.M. Chen, R. Ramachandran, *Nanoscale*, 14 (2022) 1250–1263.
3. D. Gaso-Sokac, M. Habuda-Stanic, V. Basic, D. Zobundzija, *Croat. J. Food Sci. Technol.*, 9 (2017) 204–210.
4. P. McGettigan, D. Henry, *PLoS Med.*, 10 (2013).
5. M. Dolatabadi, S. Ahmadzadeh, M.T. Ghaneian, *Environ. Prog. Sustain. Energy*, 39 (2020).
6. N. Cimolai, *Expert Rev. Clin. Pharmacol.*, 6 (2013) 289–305.
7. M. Balali-Mood, A.T. Proudfoot, J.A.J.H. Critchley, L.F. Prescott, *Lancet*, 317 (1981) 1354–1356.
8. M. Parolini, *Sci. Total Environ.*, 740 (2020) 140043.
9. I. Niopas, K. Mamzoridi, *J. Chromatogr. B Biomed. Sci. Appl.*, 656 (1994) 447–450.
10. E.G. Zisimopoulos, G.Z. Tsogas, D.L. Giokas, N.I. Kapakoglou, A.G. Vlessidis, *Talanta*, 79 (2009) 893–899.
11. N.A. Alarfaj, S.A. Altamimi, L.Z. Almarshady, *Asian J. Chem.*, 21 (2009) 217–226.
12. F.A. Aly, S.A. Al-Tamimi, A.A. Alwarthan, *Anal. Chim. Acta*, 416 (2000) 87–96.
13. T. Pérez-Ruiz, C. Martínez-Lozano, A. Sanz, E. Bravo, *J. Chromatogr. B Biomed. Appl.*, 708 (1998) 249–256.
14. A.B. Tabrizi, *Bull. Korean Chem. Soc.*, 27 (2006) 1199–1202.
15. M. Hasanzadeh, N. Shadjou, L. Saghatforoush, J.E.N. Dolatabadi, *Colloids Surfaces B Biointerfaces*, 92 (2012) 91–97.
16. S.D. Bukkitgar, N.P. Shetti, D.S. Nayak, G.B. Bagehalli, S.T. Nandibewoor, *Der Pharma Chem.*, 6 (2014) 258–268.
17. Y. Akbarian, M. Shabani-Nooshabadi, H. Karimi-Maleh, *Sensors Actuators, B Chem.*, 273 (2018) 228–233.
18. N.P. Shetti, D.S. Nayak, S.J. Malode, R.R. Kakarla, S.S. Shukla, T.M. Aminabhavi, *Anal. Chim. Acta*, 1051 (2019) 58–72.
19. J. Lee, N. Son, N.K. Park, H.J. Ryu, J.I. Baek, Y. Sohn, J.Y. Do, M. Kang, *Electrochim. Acta*, 379 (2021) 138168.
20. H. Tang, M. Jiang, Y. Zhang, X. Lai, C. Cui, H. Xiao, S. Jiang, E. Ren, Q. Qin, R. Guo, *Electrochim. Acta*, 354 (2020) 136760.
21. Y. Zhang, S. Yun, C. Wang, Z. Wang, F. Han, Y. Si, *J. Power Sources*, 423 (2019) 339–348.
22. D. Liu, Z. Jin, H. Li, G. Lu, *Appl. Surf. Sci.*, 423 (2017) 255–265.
23. T.E. Balaji, H. Tanaya Das, T. Maiyalagan, *ChemElectroChem*, 8 (2021) 1723–1746.
24. R. Sundaresan, V. Mariyappan, S.M. Chen, M. Keerthi, R. Ramachandran, *Colloids Surfaces A Physicochem. Eng. Asp.*, 625 (2021) 126889.
25. F. Fu, Z. Cheng, J. Lu, *RSC Adv.*, 5 (2015) 85395–85409.
26. C.M. Jiang, G. Segev, L.H. Hess, G. Liu, G. Zaborski, F.M. Toma, J.K. Cooper, I.D. Sharp, *ACS Appl. Mater. Interfaces*, 10 (2018) 10627–10633.
27. L. Liu, Y.-C. Wu, P. Rozier, P.-L. Taberna, P. Simon, *Research*, 2019 (2019) 1–11.
28. M.M. Teixeira, R.C. De Oliveira, M.C. Oliveira, R.A. Pontes Ribeiro, S.R. De Lazaro, M.S. Li, A.J. Chiquito, L. Gracia, J. Andrés, E. Longo, *Inorg. Chem.*, 57 (2018) 15489–15499.
29. H. Saji, Y. Nakayama, T. Yamadaya, M. Asanuma, *Phys. Lett. A*, 34 (1971) 349–350.
30. L. Pei, Y. Pei, Y. Xie, C. Fan, D. Li, Q. Zhang, *J. Mater. Res.*, 27 (2012) 2391–2400.

31. V. Mariyappan, S.M. Chen, K. Murugan, A. Jeevika, T. Jeyapragasam, R. Ramachandran, *Colloids Surfaces A Physicochem. Eng. Asp.*, 637 (2022) 128271.
32. L.Z. Pei, Y.Q. Pei, Y.K. Xie, C.Z. Yuan, D.K. Li, Q.F. Zhang, *CrystEngComm*, 14 (2012) 4262–4265.
33. V. Mariyappan, M. Keerthi, S.M. Chen, *J. Agric. Food Chem.*, 69 (2021) 2679–2688.
34. V. Mariyappan, M. Keerthi, S.M. Chen, T. Jeyapragasam, *J. Colloid Interface Sci.*, 600 (2021) 537–549.
35. E.M. Kirchner, T. Hirsch, *Microchim. Acta*, 187 (2020).
36. Z. Ji, Y. Wang, J. Yang, X. Shen, Q. Yu, L. Kong, H. Zhou, *RSC Adv.*, 6 (2016) 107709–107716.
37. M. Hojamberdiev, M.S. Bozgeyik, A.M. Abdullah, M.F. Bekheet, G. Zhu, Y. Yan, Y. Xu, K. Okada, *Mater. Res. Bull.*, 48 (2013) 1388–1396.
38. N. Karuppusamy, V. Mariyappan, S.M. Chen, M. Keerthi, R. Ramachandran, *Colloids Surfaces A Physicochem. Eng. Asp.*, 626 (2021) 127094.
39. R. Monsef, M. Salavati-Niasari, *Biosens. Bioelectron.*, 178 (2021) 113017.
40. S. Bonyadi, K. Ghanbari, M. Ghiasi, *New J. Chem.*, 44 (2020) 3412–3424.
41. P. Tarlekar, S. Chatterjee, *J. Electroanal. Chem.*, 803 (2017) 51–57.
42. A. Babaei, B. Khalilzadeh, M. Afrasiabi, *J. Appl. Electrochem.*, 40 (2010) 1537–1543.
43. T. Madrakian, E. Haghshenas, M. Ahmadi, A. Afkhami, *Biosens. Bioelectron.*, 68 (2015) 712–718.
44. T.Y. Huang, C.W. Kung, H.Y. Wei, K.M. Boopathi, C.W. Chu, K.C. Ho, *J. Mater. Chem. A*, 2 (2014) 7229–7237.
45. V. Mariyappan, M. Keerthi, S.-M. Chen, G. Boopathy, *J. Electrochem. Soc.*, 167 (2020) 117506.
46. V. Mariyappan, N. Karuppusamy, S.M. Chen, P. Raja, R. Ramachandran, *Microchim. Acta*, 189 (2022).